$Na_2FeP_2O_7$ as a Promising Iron-Based Pyrophosphate Cathode for Sodium Rechargeable Batteries: A Combined Experimental and Theoretical Study

Heejin Kim, R. A. Shakoor, Chansun Park, Soo Yeon Lim, Joo-Seong Kim, Yong Nam Jo, Woosuk Cho, Keiichi Miyasaka, Ramazan Kahraman, Yousung Jung, and Jang Wook Choi**

Considering the promising electrochemical performance of the recently reported pyrophosphate family in lithium ion batteries as well as the increasing importance of sodium ion batteries (SIBs) for emerging large-scale applications, here, the crystal structure, electrochemical properties, and thermal stability of $Na_2FeP_2O_7$, the first example ever reported in the pyrophosphate family for SIBs, are investigated. $Na_2FeP_2O_7$ maintains well-defined channel structures (triclinic framework under the *P1* space group) and exhibits a reversible capacity of ≈90 mAh g^{-1} with good cycling performance. Both quasi-equilibrium measurements and first-principles calculations consistently indicate that $Na_2FeP_2O_7$ undergoes two kinds of reactions over the entire voltage range of 2.0–4.5 V (vs Na/Na^+): a single-phase reaction around 2.5 V and a series of two-phase reactions in the voltage range of 3.0–3.25 V. $Na_2FeP_2O_7$ shows excellent thermal stability up to 500 °C, even in the partially desodiated state ($NaFeP_2O_7$), which suggests its safe character, a property that is very critical for large-scale battery applications.

1. Introduction

Lithium ion batteries (LIBs) have been successfully used for various applications represented by mobile electronics and hybrid electrical vehicles. Despite the widespread use of LIBs, batteries based on alternative carrier ions such as sodium (Na) ions could be more suitable for large-scale energy storage systems (ESSs) in which the abundance and cost of raw materials become more critical.[1,2] For reference, material price for sodium ion batteries (SIBs) is estimated to be 30 times lower than that of LIBs.[3] Moreover, SIBs are electrochemically analogous to LIBs because the systems are based on similar alkali carrier ions. Thus, the well-established knowledge and experience developed for LIBs could be utilized, although there are known differences between Li and Na such as the size and coordination preference, which could lead to different electrochemical consequences.[3] Despite the various advantages and opportunities, SIBs are required to overcome their drawbacks such as lower energy densities and inferior kinetics compared to those of LIBs, most of which originate from the larger size of the carrier ion.

Recently, among various polyanion-based LIB cathodes, pyrophosphate-based materials demonstrated good electrochemical and thermal properties and have thus received considerable attention.[4–7] The Yamada group found that $Li_2FeP_2O_7$ exhibits a redox potential at 3.5 V vs. Li/Li^+ while showing a reversible capacity of ≈120 mAh g^{-1}.[5] The Whittingham group expanded to $Li_2MP_2O_7$ ($M = Fe_xMn_{1-x}$, $0 \le x \le 1$) but observed that the addition of Mn decreases the specific capacity severely.[6] For the similar mixed metal pyrophosphate, the Yamada group observed the Mn effect on raising the Fe potential.[7] Also, the Kang group examined $Li_2CoP_2O_7$, but it turned out that its operational potential (≈5 V vs. Li/Li^+) is too high for typical LIB electrolytes to remain stable.[2] The Kang group additionally observed that the lithium pyrophosphate family exhibits good thermal stability.[2] Furthermore, the pyrophosphate family shows 0.1–0.2 V higher redox potentials for most transition metals compared to those based on other polyanions, which is desirable for high cell energy densities.[2,5]

Motivated by the potential significance of SIBs for large-scale ESSs as well as the promising electrochemical and thermal properties of the lithium pyrophosphate family, herein, we investigate a sodium version of Fe-based pyrophosphate, $Na_2FeP_2O_7$, as an SIB cathode. In the crystal structure viewpoint, even for the same Fe-based pyrophosphate, the change of

H. Kim, C. Park, S. Y. Lim, J.-S. Kim, Dr. K. Miyasaka, Prof. Y. Jung, Prof. J. W. Choi
Graduate School of EEWS (WCU)
KAIST Institute NanoCentury
Korea Advanced Institute of Science and Technology (KAIST)
Yuseong-gu, Daejeon, 305-701, Republic of Korea
E-mail: ysjn@kaist.ac.kr; jangwookchoi@kaist.ac.kr
Dr. R. A. Shakoor, Prof. R. Kahraman
Department of Chemical Engineering
College of Engineering
Qatar University
P.O.Box: 2713, Doha, Qatar
Y. N. Jo, Dr. W. Cho
Advanced Batteries Research Center
Korea Electonics Technology Institute (KETI)
Bundang-gu, Seongnam-si, Gyeonggi-do, 463-816, Republic of Korea

DOI: 10.1002/adfm.201201589

alkali ions from Li to Na results in different crystal frameworks: while $Li_2FeP_2O_7$ adopts the monoclinic structure,[5] $Na_2FeP_2O_7$ adopts the triclinic structure. Nonetheless, as described below, $Na_2FeP_2O_7$ still exhibits a clear electrochemical activity in the potential range of 2–4.5 V vs. Na/Na^+ with a reversible capacity of ≈90 mAh g^{-1} corresponding to the activity of almost one Na ion per each $Na_2FeP_2O_7$. Moreover, $Na_2FeP_2O_7$ mimics $Li_2FeP_2O_7$ in that both materials show outstanding thermal stability up to 500 °C even in the partially charged states ($NaFeP_2O_7$). To date, a variety of Na-based pyrophosphates such as $NaFeP_2O_7$,[8,9] $NaVP_2O_7$,[10] $NaMoP_2O_7$,[11] $Na_2MnP_2O_7$,[12,13] $Na_2CoP_2O_7$,[14–16] $Na_2ZnP_2O_7$[17] and $Na_2CuP_2O_7$[18] have been investigated. While these pyrophosphate materials adopt different crystal structures depending on transition metals, most of them contain open frameworks that could facilitate efficient diffusion of Na ions for battery operation. Nevertheless, to the best of our knowledge, none of these materials have been reported as SIB electrode materials. Surprisingly, in the case of $Na_2FeP_2O_7$, neither its synthesis nor crystal structure has been reported.

2. Results and Discussion

2.1. Structural Characteristics

The family of $Na_2MP_2O_7$ (M = Mn, Co, Cu, Zn) adopts different crystal structures and space groups depending on the transition metals involved: When M = Zn,[19] Mn,[13] and Cu (both α and β phases),[18] the structures take the tetragonal, triclinic, and monoclinic crystal systems, respectively. Also, some compounds in this family show allotropic behavior. For example, $Na_2CoP_2O_7$ could adopt both tetragonal (blue)[14,16] and triclinic (rose)[15] structures depending on synthetic procedures. As a comparison, the X-ray diffraction (XRD) characterization (**Figure 1**a) indicates that $Na_2FeP_2O_7$, the material of interest in this study, is isostructural with $Na_2CoP_2O_7$-*rose*, adopting the triclinic structure under the space group *P1*.[15] When fitted, the XRD peaks of $Na_2FeP_2O_7$ match well with the data of $Na_2CoP_2O_7$-*rose* and thus imply that highly crystallized and phase-pure $Na_2FeP_2O_7$ was synthesized through a simple and commercially adoptable solid state synthesis. The lattice parameters attained from the XRD analyses are tabulated in **Table 1** and are also compared to those of $Na_2CoP_2O_7$-*rose*. The lattice parameters of $Na_2FeP_2O_7$ agree well with $Na_2CoP_2O_7$-*rose*. However, slight variations in the lattice parameters were observed: as the transition metal changes from Co to Fe, the lattice parameters are increased along the *b*- and *c*-directions by 0.07 and 0.01 Å, respectively, whereas the lattice parameter is decreased along the *a*-direction by 0.04 Å. These variations may be due to the ionic radii

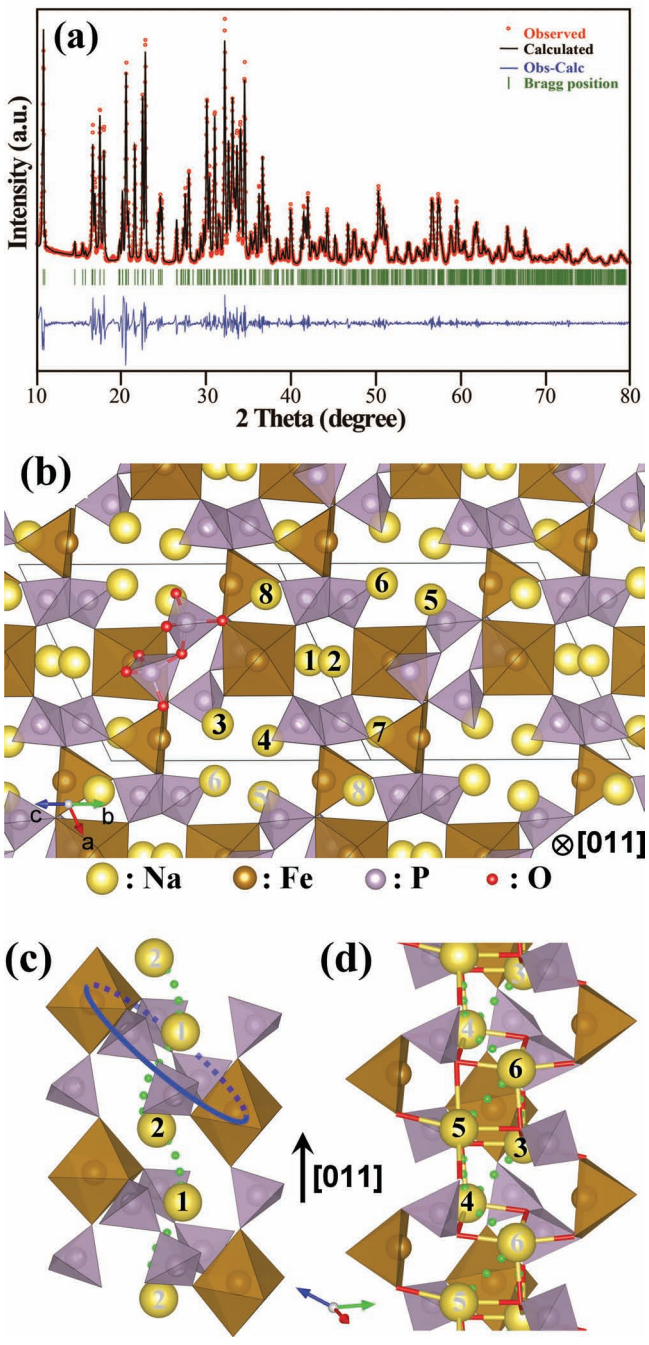

Figure 1. a) The XRD spectrum and whole pattern fitting of $Na_2FeP_2O_7$ (R_p = 5.98, R_{wp} = 8.99, χ^2 = 10.8). b) The crystal structure of $Na_2FeP_2O_7$ projected along the [011] direction showing the different sodium sites and the arrangement of octahedral and polyhedral units. The sodium migration channels for c) the Na1 and Na2 sites and d) the Na3–Na6 sites.

Table 1. The lattice parameters of $Na_2CoP_2O_7$ and $Na_2FeP_2O_7$.

Material	a [Å]	b [Å]	c [Å]	α [°]	β [°]	γ [°]	Structure	ref.
$Na_2CoP_2O_7$	9.74	10.94	12.29	148.78	121.76	68.38	Triclinic-*P1*	[15]
$Na_2FeP_2O_7$	9.70	11.01	12.30	148.59	121.61	68.55	Triclinic-*P1*	this work

difference of the transition metal (Co^{2+}: 0.745 Å, Fe^{2+}: 0.78 Å for high-spin state within six-fold coordination).[20] The comparative XRD analyses (Figure S1, Supporting Information) of $Na_2FeP_2O_7$ before and after the carbon coating and subsequent annealing confirm that the original pure phases are maintained throughout the additional treatments. Hereafter, the carbon-coated and annealed sample before any electrochemical processes will be referred to as the pristine sample.

The crystal structure of $Na_2FeP_2O_7$ can be described by a framework consisting of the metal polyhedra (FeO_6 and FeO_5) and the bridging pyrophosphate P_2O_7 groups (Figure 1b). All metal and phosphate polyhedra are connected to each other with sharing corners that create various channel structures for Na ion migration as described below. As for Na sites, there are 8 Na sites (Na1–Na8) in the unit cell, which can be categorized into three groups (A, B, and C) based on their chemical and structural environments: In the group A, Na1 and Na2 are located in a small channel along the [011] direction. Na1 (Na2) is in a tetrahedral (pyramidal) site sharing two corners (edges) with the neighboring Fe octahedra. A pair of Na1 and Na2 are separated by a "ring" consisting of two Fe(P_2O_7) groups. It can be viewed that in Figure 1c, the grey-colored pair of Na1 and Na2 are separated from the black-colored pair of Na1 and Na2 by the denoted blue ring. These rings are then replicated to form a 1D Na channel. For the group B, Na3–Na6 are located in a larger tunnel and linked to each other by sharing edges along the same channel direction (Figure 1d). In the group C, a pair of Na7 and Na8 are located in pyramidal sites, and can migrate to each other through the $[Fe(P_2O_7)]_2$ ring. However, the Na migration from one pair to the next pair is limited by high migration barriers (>2.5 eV). Therefore, Na7 and Na8 are not expected to form any independent channels but instead form 2D migration paths to the neighboring channels such as Na7–Na2 and Na8–Na5. The migration barrier at each Na site would affect the kinetics of Na diffusion and will be discussed in Section 2.4.

In order to confirm the phase purity of the synthesized compound, inductively coupled plasma (ICP) compositional analyses were carried out and the results are presented in Table S1 (Supporting Information). The atomic ratio of Na:Fe:P = 1.94:0.94:2 is consistent with the stoichiometric ratio of the designated compound and thus verifies again the validity of the solid state reaction. The formation of the proper $Na_2FeP_2O_7$ phase was also confirmed by Fourier-transform infrared spectroscopy (FT-IR) analyses (Figure S2, Supporting Information). The presence of symmetric and anti-symmetric vibrations at 738 and 913 cm^{-1} indicates P–O–P bonds in the pyrophosphate groups. The O–P–O and P–O vibrations observed at other waver numbers can be attributed to PO_3 bonds in $(P_2O_7)^{4-}$. These findings are consistent with the previous report on the pyrophosphate family.[6] **Figure 2**a,b show the SEM images of $Na_2FeP_2O_7$ for the as-synthesized and the carbon-coated samples. These images indicate that the as-synthesized powders show relatively larger particle sizes of ≈1–2 μm, but the sizes become smaller after the carbon coating due to the milling effect of grinding balls. A transmission electron microscopy (TEM) image (Figure 2c) clearly confirms the formation of conductive carbon layers with thicknesses of 15–20 nm.

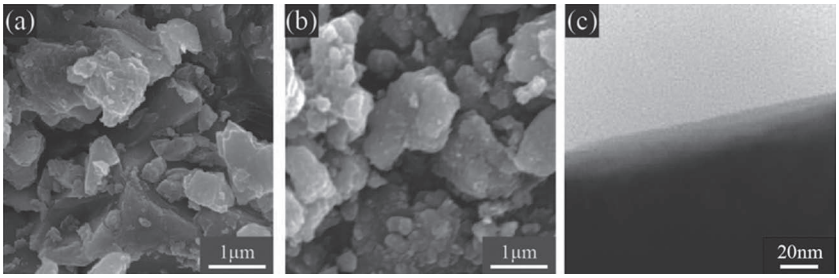

Figure 2. SEM images of $Na_2FeP_2O_7$ a) after the solid state synthesis and b) after the additional carbon-coating and annealing at 600 °C for 10 h under argon flow. c) A TEM image of the carbon-coated particle shows the formation of a carbon layer on the pristine powder.

2.2. Potential Profile and Capacity

As a means to gain a deep insight into the electrochemical reactions of $Na_2FeP_2O_7$ during charging and discharging processes, galvanostatic intermittent titration technique (GITT) analyses were conducted. The quasi-open circuit potential (QOCP) profiles measured at C/20 during the first and second cycles are presented in **Figure 3**a,b. From these profiles, following points are noteworthy:

1) In the first cycle, the discharge QOCP curve shows a new plateau around 2.5 V that did not appear during the charge. This new plateau at 2.5 V is consistently observed in the subsequent cycles and should thus be associated with the robust and distinct Na intercalation/deintercalation sites. The existence of this plateau is also consistent with the result of density functional theory (DFT) calculations described below. While the absence of this plateau during the charge in the first cycle is due primarily to the higher open circuit voltage (OCV) around 2.92 V, it is anticipated that this high OCV is reflective of the imperfect crystal structure of the as-synthesized $Na_2FeP_2O_7$, and is discussed further in the last paragraph in this section. The high OCVs were repeatedly observed over multiple samples.
2) Although the charging profiles of the first and second cycles are different, the discharging processes are almost identical and reversible over 80 cycles (Figure S3, Supporting Information). For the first and second cycles, discharging capacities of 84 and 83 mAh g^{-1} were obtained from Figure 3, which indicate that 0.87 and 0.86 Na ions are electrochemically active for each $Na_2FeP_2O_7$. For reference, the theoretical capacity for the activity of one Na per each formula unit of $Na_2FeP_2O_7$ is 97 mAh g^{-1}.
3) In both the first and second cycles, the charging profiles show apparently two distinct regions: the low voltage region (2.0–3.25 V) with small overpotentials and the high voltage region (3.25–4.5 V) with large overpotentials. The details of the high polarization region will be discussed more in the next section.

4) The different electrochemical features observed in the first cycle are attributed to the Na defects of the initial structure.

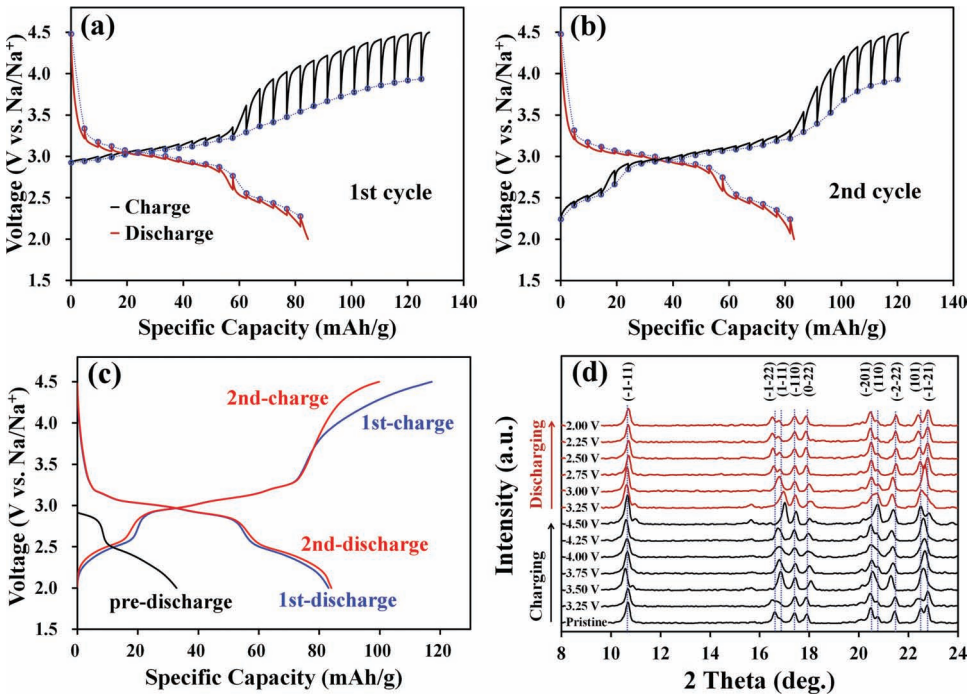

Figure 3. QOCP curves of $Na_2FeP_2O_7$ measured at C/20 in a) the first and b) the second cycles. c) The voltage profiles at a C/20 rate, starting with discharge (pre-discharge). d) Electrochemical ex situ XRD analyses data of $Na_2FeP_2O_7$ in the first charging and discharging processes.

Figure 3c shows the voltage profiles starting with the discharge (pre-discharge). In the pre-discharge profile, the 2.5 V plateau corresponding to the empty Na1 sites is clearly visible, indicating that the empty Na1 sites are filled during the pre-discharge. Also, the discharge profiles in the subsequent first and second cycles exhibit almost identical plateaus around this potential to that of the pre-discharge, again confirming the Na defect sites of the pristine $Na_2FeP_2O_7$. The similar XRD patterns between the pristine state and the partially deintercalated state at 2.75 V during discharge (Figure 3d) additionally support the Na deficiency in the pristine state. The Na defects in the pristine state can be attributed to the spontaneous extraction of Na ions due to the reaction of the compound with moisture in atmosphere.[21–23] This reaction is likely to take place during the ball milling and annealing processes in the preparation of the active material. In fact, a merging between the (101) and (-1-21) peaks was observed for the samples that went through ball milling and annealing processes (Figure S1b, Supporting Information), which was also detected during the Na extraction in the desodiation as shown in Figure 3d and Figure S4 (Supporting Information).

2.3. Phase Behavior and Plateau Location

The ex situ XRD characterization during the first cycle (Figure 3d) suggests that $Na_2FeP_2O_7$ undergoes successive biphasic transitions (including both two-phase and single-phase reactions) going through various intermediate phases. The phenomena typically observed in two-phase reactions such as growth of new peaks and simultaneous abatement of existing peaks were not observed throughout the entire cycle. Instead, some peaks experience peak merging and splitting, although they recover their original shapes after a full cycle. These phenomena suggest that the observed biphasic transitions are the first-order phase transition with preserving the overall framework of $Na_2FeP_2O_7$. The voltage step in our ex situ XRD measurements might be too large to identify all of existing intermediate phases. Nevertheless, our electrochemical analyses as well as DFT calculations indicate a consistent picture of the structural change based on such phase behavior.

In **Figure 4**a, four different plateaus were identified in the quasi-equilibrium potential curve during the charge in the second cycle (Figure 3b), consistent with the potentiostatic intermittent titration technique (PITT) measurements (Figure S5, Supporting Information). These plateaus are located at 2.52, 2.99, 3.08, and 3.24 V. Cyclic voltammetry (CV) data also consistently exhibit peaks at the same locations as denoted in Figure 4b, implying that Na sites with four different energy levels are involved in the electrochemical reaction of $Na_2FeP_2O_7$. Among the four separated peaks appearing in the CV data, the broad peak observed at the lowest potential of 2.52 V is likely to reflect the single-phase reaction in the beginning of the charge.[24] To identify the phase behaviors of the rest three peaks overlapped around 3 V, we further investigated the system by employing theoretical calculations.

The formation energy for each composition (i.e., x in $Na_xFeP_2O_7$, $1 \le x \le 2$) was first assessed. Connecting the lowest formation energy along the composition variable x forms a energy convex hull (Figure 4c).[25] The final voltage at

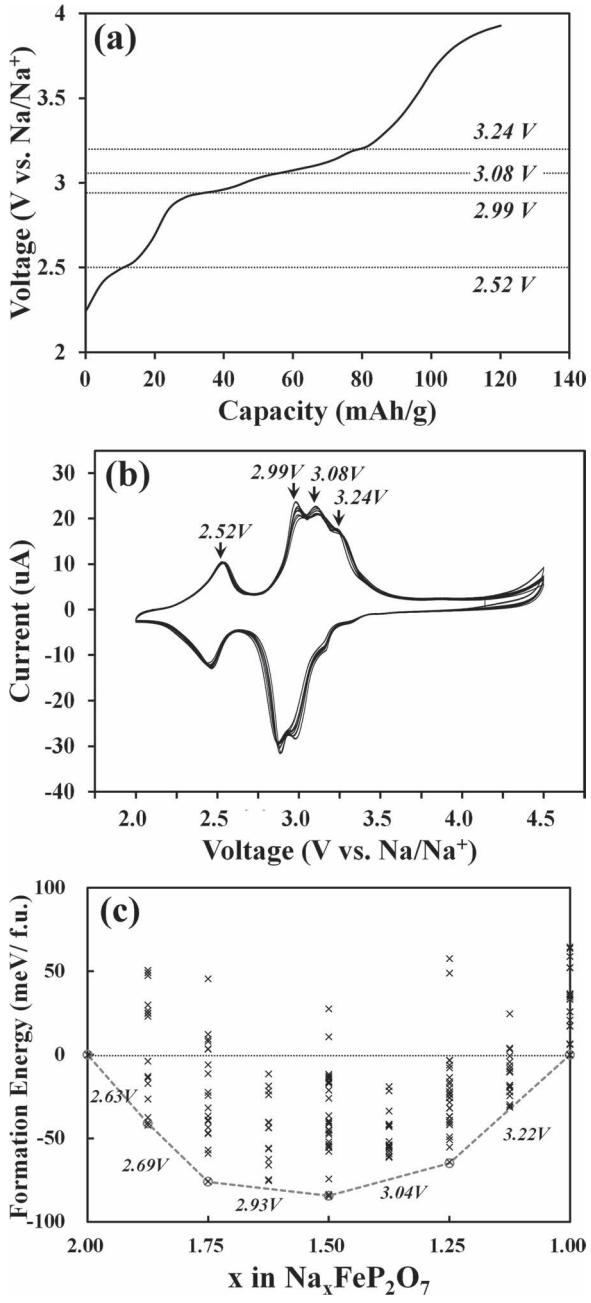

Figure 4. a) The quasi-equilibrium potentials obtained from the charge in the second cycle in the Figure 3b with the observed potentials denoted. b) The CV data measured at a scan rate of 0.05 mV s^{-1}. c) A calculated formation energy hull and a series of potentials for consecutive compositional intervals.

each compositional interval was obtained from the Boltzmann weighted energy difference between the two adjacent compositions. See the Experimental Section for calculation details. In our calculation regimes, we can conclude the following points:

1) In the range of $1 \le x \le 2$, three intermediate phases ($x = 1.75$, 1.50, and 1.25) and four biphasic transitions were identified, which is consistent with our CV and QOCP measurements. In terms of the plateau locations, the calculated voltages of 2.63–2.69, 2.93, 3.04, and 3.22 V match well with those observed experimentally in the second cycle (2.52, 2.99, 3.08, and 3.24 V).
2) The lowest potential plateau at ≈2.5 V is identified as the single phase reaction, while the remaining three transitions are associated with undergoing the two-phase reaction. In the range of $1.75 \le x \le 2.0$, the minimum energy points constitute a downward convex curve, indicating that the phase separation to the two end-points ($x = 1.75$ and 2.0), i.e., two-phase reaction, is not energetically favorable. By contrast, in other compositional ranges of $1.0 \le x \le 1.75$, minimum energy points constitute a series of upward convex curves, suggesting that the two-phase mode is preferred for each composition period. For further clarification of the phase behaviors, we performed additional CV measurements at a slower cycle rate (Figure S6, Supporting Information). Compared to the original CV data (Figure 4b), upon lowering the scan rate, the lowest peak is unaltered, however, three peaks around 3 V become clearly sharper. These results support that the phase transition at the lowest voltage plateau is the single-phase reaction, while the other three transitions at the higher voltage plateaus are the two-phase reactions,[24] consistent with the calculations.
3) The simulated XRD patterns (Figure S4, Supporting Information) using the calculated minimum energy structures at different x values successfully reproduce the experimentally observed spectral changes, verifying the preserved framework over the entire potential range as well as the consistent view on this compound in the structural and electrochemical perspectives between experimental and theoretical investigations.

2.4. Na Extraction and High Polarization

According to our DFT calculations, the 2.5 V plateau is associated with the first Na extraction at the Na1 site in Figure 1a since the energy of the Na1 site is calculated to be higher (more easily extractable) by 0.1–0.8 eV compared to those of other Na2–Na8 sites. The migration barrier required for the extraction of Na1 (0.48 eV) along the [011] channel direction is also lower than those of other extraction channels (0.54–0.67 eV) as illustrated in **Figure 5**. Thus, Na1 is the most easily accessible Na site for deintercalation, both thermodynamically and kinetically. The DFT calculations also indicate that the plateaus around 3 V are associated with Na sites in the group B and C (Na3–Na8). As shown in Figure 5, all Na ions in these groups can be extracted through the 1D channels or/and 2D pathways (red line) with comparable barriers below 0.54 eV. It is anticipated that the 2D connections enable Na diffusion to be less sensitive to anti-site defects because alternative pathways free of defects could always be available.

As pointed out in the QOCP data (Figure 3a,b), the potential profiles exhibit large polarization during the charging process above 3.25 V. The structural changes of electrode material observed in the ex situ XRD measurements (Figure 3d)

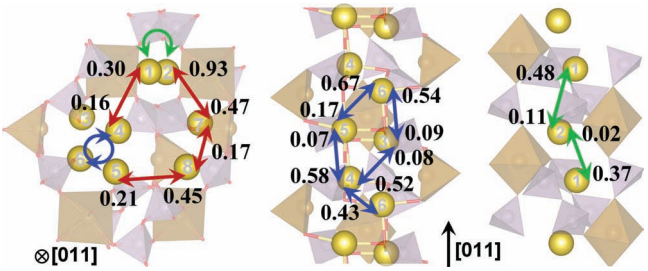

Figure 5. The calculated Na ion migration barriers (in eV) for the $Na_2FeP_2O_7$. The arrowhead and the number next to it indicate the direction of Na-migration and the corresponding migration barrier (either forward or backward). For Na-migrations between the two symmetrically equivalent sites, forward and backward migrations have the same barriers, thus only one number is denoted in the middle of the arrow. Color code: red for 2D migration paths, and green (Na1 and Na2 sites) and blue (Na3–Na6 sites) for the outward channels. Migration barriers along the [011] channel direction (green and blue) are shown separately on the two rightmost panels for clarity.

suggest the Na extraction at this high voltage region. However, we can exclude the extraction of more than one Na ions since it should be accompanied by the Fe^{3+}/Fe^{4+} redox reaction which has a substantially higher redox potential (≈5 V) over the measurement condition based on our calculations (Figure S7, Supporting Information). Therefore, the applied currents are consumed by both Na extraction and unwanted side reactions since the charging capacities (130 mAh g^{-1}) are higher than the theoretical capacity (97 mAh g^{-1}). While the origins of the side reactions in the first cycle are currently speculated to be associated with the electrolyte decomposition, further investigation is clearly required for complete understanding.

2.5. Cycle and Rate Performance

The cycling performance of $Na_2FeP_2O_7$ measured at a C/20 rate is displayed in **Figure 6**a. The reversible capacity is preserved after 80 cycles (92 mAh g^{-1}), suggesting that Na insertion/extraction within this compound is quite reversible. The rate capability data of $Na_2FeP_2O_7$ is presented in Figure 6b. It is found that as the c-rate increases 20-fold from C/20 to 1C, the specific capacity decreases from 87 to 65 mAh g^{-1}, exhibiting decent capacity retention such that 74% of the initial capacity is maintained. However, the capacity decreases more significantly with further increase in the c-rate. When the c-rate increases from 1C to 4C, the capacity decreases from 65 to 35 mAh g^{-1}. This relatively inferior capacity retention at higher c-rates seemingly suggests that this compound holds moderate electric conductivity and thus suffers from the drawback of its particle dimensions in micrometers. It is expected that the rate capability would be improved drastically by nanosizing of the particles.

2.6. Thermal Stability

$Na_2FeP_2O_7$ exhibits excellent thermal stability in both the pristine and partially desodiated states ($NaFeP_2O_7$). When heated

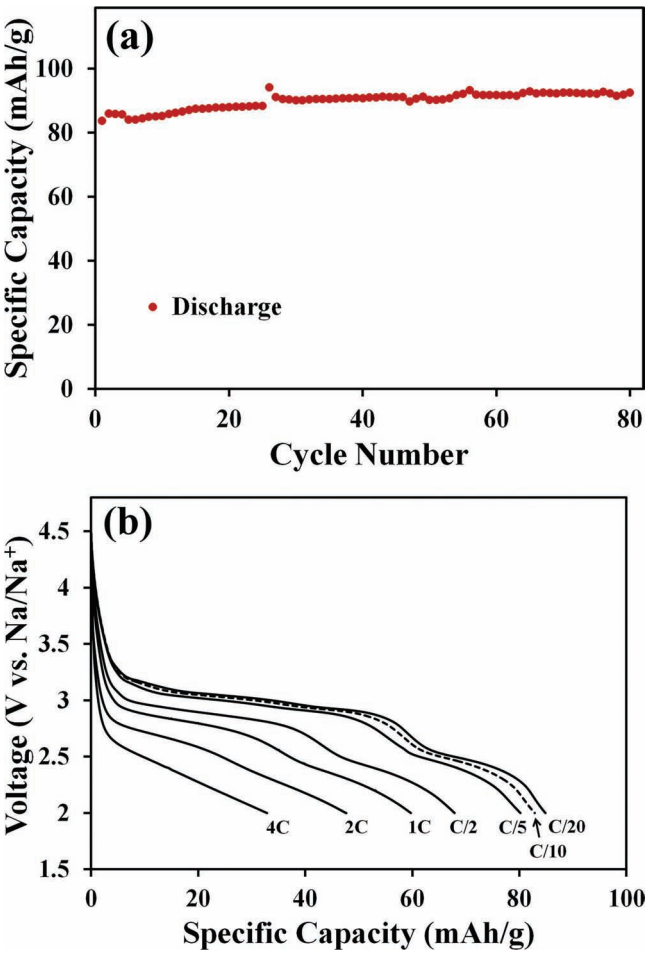

Figure 6. a) Cycling performance of $Na_2FeP_2O_7$ measured at C/20. b) Rate capability data measured at C/20 for charging and at various rates for discharging.

up to 550 °C, thermogravimetric analysis (TGA) data indicate that both the pristine and partially desodiated states lose negligible weight loss of 2–5% (**Figure 7**). The weight loss of the partially desodiated sample is indeed comparable to that of the Li counterpart, $LiFeP_2O_7$, which shows 5% weight loss in the same temperature range.[2] Also, differential thermal analysis (DTA) profiles for both states do not show any noticeable exo/endothermic peaks in the same temperature range. In fact, DTA data indicate that the thermal stability of the partially desodiated state turns out to be superior to that of the Li-based counterpart ($LiFeP_2O_7$), which shows a high exothermic peak around 550 °C.[2] In order to see more detailed thermal properties focusing on the phase stability, in situ thermal XRD characterization was conducted. As shown in **Figure 8**a, the pristine sample does not exhibit any signal of phase transformation up to 550 °C. Only peak shifts toward lower 2θ values were observed, which is attributed to the expansion of the unit cell upon heating. In the case of the partially desodiated sample ($NaFeP_2O_7$), similar trend was observed up to 500 °C (Figure 8b). The new phase starts to appear at 550 °C and is

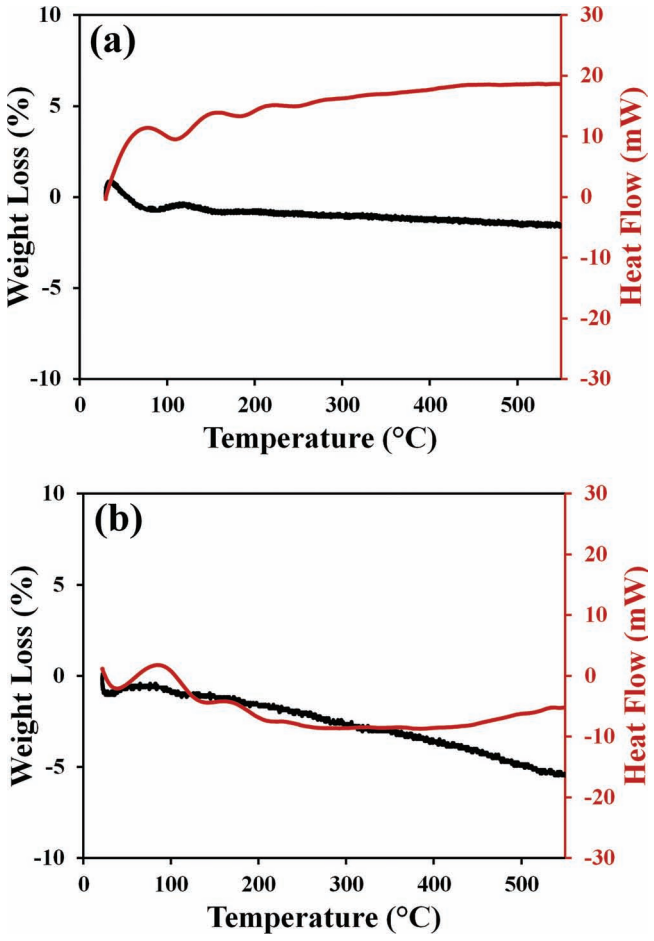

Figure 7. TGA/DTA data for a) the pristine state ($Na_2FeP_2O_7$) and b) the partially desodiated state ($NaFeP_2O_7$) recorded at a rate of 10 °C min^{-1} in the presence of argon.

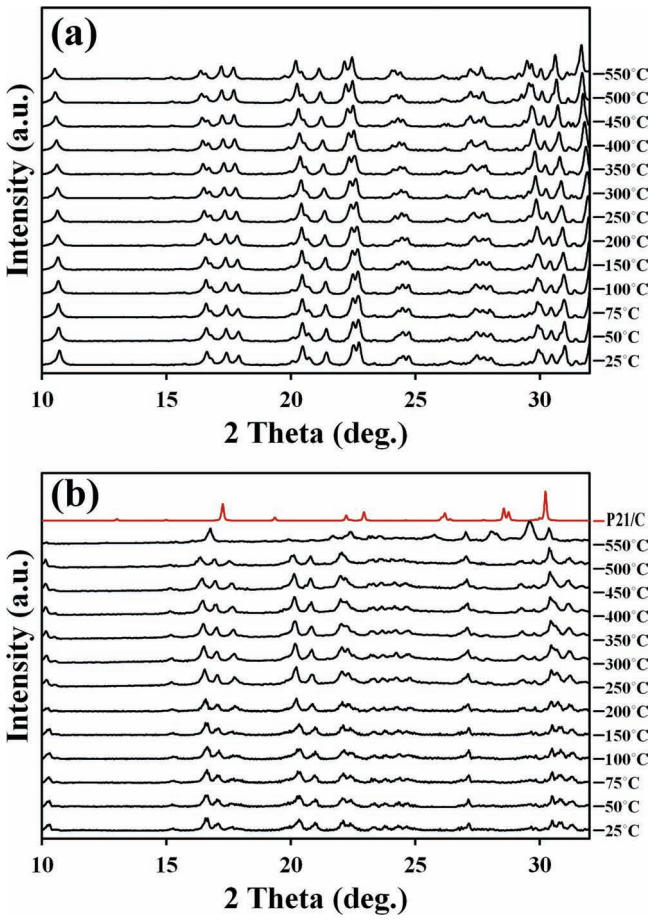

Figure 8. In situ thermal XRD analyses performed in the temperature range of 25–550 °C for a) the pristine state ($Na_2FeP_2O_7$) and b) the partially desodiated state ($NaFeP_2O_7$). The XRD pattern (red line) of the monoclinic ($P2_1/c$ space group) $NaFeP_2O_7$ is also included in (b) for comparison.

indexed to the monoclinic ($P2_1/c$ space group) $NaFeP_2O_7$.[8] For clear comparison, the reference pattern of monoclinic $NaFeP_2O_7$ is also presented in Figure 8b (red line). The reference peaks and those of the desodiated at 550 °C match well except that those of the desodiated at 550 °C are shifted toward smaller 2θ values perhaps due to the thermal expansion at high temperatures. Overall, the newly developed $Na_2FeP_2O_7$ promises superior thermal stability compared to that of other cathode materials including olivine family that is known to be thermally stable due to the P–O bonding. In the pristine states, $LiMnPO_4$,[26] $LiFePO_4$[27] were reported to be thermally stable up to 400 °C. For the charged states, the thermal stability of $NaFeP_2O_7$ is substantially better than those of $MnPO_4$ (150–200 °C),[26,28] and $CoPO_4$ (≈250 °C),[29] and is comparable to that of $FePO_4$ (≈500 °C).[30]

3. Conclusions

We report the structure, electrochemical, and thermal properties of $Na_2FeP_2O_7$ as a SIB cathode material. The material was synthesized through the conventional solid state synthesis. The structural characterization indicates that $Na_2FeP_2O_7$ adopts the triclinic framework under the *P1* space group. Utilizing the well-developed channel structures, $Na_2FeP_2O_7$ exhibits promising electrochemical behavior based on the activation of the Fe^{3+}/Fe^{2+} redox couple. The material shows a reversible capacity of ≈90 mAh g^{-1} while exhibiting two distinct plateaus in the potential range of 2.0–4.5 V (vs Na/Na^+): one at 2.5 V based on a single-phase mode and the others in the potential range of 3.0–3.25 V based on consecutive two-phase reactions. Moreover, $Na_2FeP_2O_7$ exhibits excellent thermal stability such that both the pristine and partially desodiated states show negligible weight loss and no phase transformation up to 500 °C. Overall, $Na_2FeP_2O_7$, as the first member ever reported in the pyrophosphate family for SIB cathodes, turns out to hold good electrochemical and thermal characteristics and could thus be a promising candidate for SIB electrodes targeting large-scale applications.

4. Experimental Section

Sample Preparation: $Na_2FeP_2O_7$ was synthesized via a solid state reaction by reacting stoichiometric amounts of the precursors

under argon flow. The stoichiometric amounts of Na_2CO_3 (Aldrich), $(NH_4)_2HPO_4$ (Aldrich) and $FeC_2O_4{\cdot}2H_2O$ (Aldrich) were first intimately mixed. The powder was then pelletized and annealed at 350 °C for 3 h in an argon atmosphere. The pellets were cooled to room temperature and were ground. The reground powders were re-pelletized and annealed at 600 °C for 6 h in an argon atmosphere to form the desired phase according to the following chemical reaction:

$$Na_2CO_3 + 2(NH_4)_2\,HPO_4 + FeC_2O_4{\cdot}2H_2O \rightarrow Na_2FeP_2O_7 + 4H_2 + 2N_2 + 3CO + 7H_2O$$

The as-synthesized powders were carbon-coated through a dry ball milling process (active material: Super P = 8:2 in weight, 24 h, 500 rpm) to improve the electrical conductivity. After the carbon coating process, the carbon-coated samples were pelletized and annealed at 600 °C for 10 h under argon flow to restore the crystallinity.

Characterization: The crystal structures of the synthesized materials were characterized by XRD (Rigaku, D/MAX-2500, Tokyo, Japan) equipped with Cu Kα radiation. XRD patterns were fitted (whole pattern fitting) using the Full Prof Software. The sizes and morphologies of powder particles were characterized by field emission SEM (FEI, Magellan400) and field emission TEM (TECNAI, Netherlands). The atomic compositions of the samples were confirmed by ICP mass spectroscopy (HP 4500). The infrared (IR) spectra of the prepared materials were recorded in the range of 2500–400 cm^{-1} using an FT-IR spectrometer (Jasco, FR/IR-4100, Japan) in the transmission mode based on the KBr pellet method. Thermal in situ XRD analyses were carried out using the aforementioned XRD characterization. The thermal in situ XRD study was performed at a heating rate of 5 °C min^{-1}, the dwell time between heating and measurement at each temperature was 3 min, and the XRD scan speed was 1° min^{-1}.

Electrochemical Characterization: Coin type half-cells (CR2032) were prepared in an argon filled glove box. Na thin disks, 1 M sodium perchlorate ($NaClO_4$) in propylene carbonate (PC), and polyethylene separators (Celgard 2400) were used as the counter electrodes, electrolyte, and separators, respectively. The separators were polydopamine-treated as previously reported to make the separator surfaces hydrophilic.[31] Slurries were prepared by mixing the carbon-coated active material (75 wt%), carbon black (15 wt%) and polyvinylidene fluoride (PVDF) (10 wt%) in *N*-methyl-2-pyrrolidone (NMP). After stirring at 25 °C overnight, the slurry was cast onto aluminum foil using the doctor blade technique. Then, the cast samples were dried in a vacuum oven at 110 °C for 2 h. The partially desodiated samples ($NaFeP_2O_7$) for thermal in situ analyses were prepared through electrochemical desodiation. During this process the cells were charged to 4.5 V, and the potential was held for 5 h. Finally, the cells were disassembled inside a glove box, washed with PC, and dried at room temperature.

Electrochemical properties were examined by GITT and galvanostatic techniques in the voltage range of 2.0–4.5 V (vs. Na/Na^+) at room temperature using a battery cycler (WonA Tech, WBCS 3000, Korea). The QOCP measurements were performed at a C/20 rate with the intermittent charge-discharge mode (1 C: each charge/discharge takes 1 h). 2 h of relaxation time was applied after each 1 h charge/discharge step. For the electrochemical ex situ XRD analyses, the samples were galvanostatically scanned at a C/20 rate and the bias was on hold for 2 h at the target potentials before the XRD measurements. The cycling performance was evaluated by galvanostatic measurement technique at a C/20 rate in the voltage range of 2.0–4.5 V.

Density Functional Calculations: We performed spin-polarized DFT calculations as implemented in the Vienna Ab-initio Simulation Package (VASP).[32] We used the Perdew-Burke-Ernzerhof (PBE) exchange-correlation functional[33] and projector-augmented wave (PAW) method.[34] For the total energy calculations, we adopted the Hubbard *U*-corrections in the rotationally invariant form proposed by Dudarev et al. to address the self-interaction energy.[35] The self-consistently calculated effective *U* value for Fe in olivine structure (4.3 eV) was used[36] for the pyrophosphate since the chemical environments for both compounds are similar in terms of the inductive effects from neighboring phosphate polyanions. A reoriented unit cell containing 8 formula units (11.0 × 13.4 × 9.6 Å) was used to minimize the interactions between neighboring periodic images. All calculations were performed in a high-spin ferromagnetic ordering. The calculated energy difference between ferromagnetic (FM) and antiferromagnetic (AFM) ordering was less than 5 meV per formula unit, implying that the magnetic structure has an insignificant effect on the energy calculations.

For the formation energy convex hull, the 30 lowest electrostatic energy configurations determined using the Ewald summation technique[37] were used as an input for geometry optimizations at each composition. Additional configurations were included by considering crystallographic symmetry to explore the ion orderings for completeness. To calculate the voltage profile from a minimum energy hull, the "ensemble" average of the total energy at each composition, $\langle E^x \rangle$, was used instead of a global minimum alone.[38]

$$\langle E^x \rangle = \sum_i E_i^x P_i^x \quad (1)$$

where E^x_i is the total energy of the given configuration and P^x_i is the probability of seeing that particular configuration given by

$$P_i^x = e^{-E_i/kT} \Big/ \sum_i e^{-E_i/kT} \quad (2)$$

In the present system, the energy difference between the minimum energy and high-lying structures at most compositions turns out to be large enough compared to the thermal energy at room temperature (kT = 25.6 meV), which makes this statistical approach insignificant. However, this Boltzmann averaged voltage gives a more physical meaning than the voltage calculated for the minimum structure alone since the experimental voltage is measured at finite temperatures. Thus, this statistical weighting is expected to become essential for cases where the energy difference between different configurations is small.

The nudged elastic band (NEB) method[39] with eight images along the Na migration path was used to evaluate the sodium migration barriers. In the NEB calculation, the *U*-correction was dropped to avoid the uncertainty that arises from the mixing of Na migration barrier with a charge transfer barrier.[40,41] A plane wave basis set with an energy cutoff of 500 eV and a 2 × 2 × 2 Monkhorst-Pack *k*-point mesh sampling[42] were used for all calculations to give well converged energy values.

Supporting Information

Supporting Information is available from the Wiley Online Library or from the author.

Acknowledgements

H.K. and R.A.S. contributed equally to this work. The authors acknowledge financial support from the National Research Foundation of Korea Grant funded by the Korean Government (MEST) (NRF-2010-0029031, NRF-2012-R1A2A1A01011970, NRF-2011-0026038) and the World Class University Program (R-31-2008-000-10055-0). They also thank KISTI supercomputing center for the generous computing time and technical support. After this manuscript was published online, the following papers, which report the same material, were noted: T. Honma, T. Togashi, N. Ito, T. Komatsu, *J. Ceram. Soc. Jpn.*, **2012**, *120*, 344 and P. Barpanda T. Ye, S.-i. Nishimura, S.-C. Chung, Y. Yamada, M. Okubo, H. Zhou, A. Yamada, *Electrochem. Commun.*, **2012**, *24*, 116.

Received: June 13, 2012
Revised: September 12, 2012
Published online: October 8, 2012

[1] M. Armand, J. M. Tarascon, *Nature* **2008**, *451*, 652.
[2] H. Kim, S. Lee, Y.-U. Park, H. Kim, J. Kim, S. Jeon, K. Kang, *Chem. Mater.* **2011**, *23*, 3930.
[3] M. D. Slater, D. Kim, E. Lee, C. S. Johnson, *Adv. Funct. Mater.* DOI: 10.1002/adfm.201200691.
[4] R. A. Shakoor, H. Kim, W. Cho, S. Y. Lim, H. Song, J. W. Lee, J. K. Kang, Y.-T. Kim, Y. Jung, J. W. Choi, *J. Am. Chem. Soc.* **2012**, *134*, 11740.
[5] S.-i. Nishimura, M. Nakamura, R. Natsui, A. Yamada, *J. Am. Chem. Soc.* **2010**, *132*, 13596.
[6] H. Zhou, S. Upreti, N. A. Chernova, G. Hautier, G. Ceder, M. S. Whittingham, *Chem. Mater.* **2010**, *23*, 293.
[7] N. Furuta, S.-i. Nishimura, P. Barpanda, A. Yamada, *Chem. Mater.* **2012**, *24*, 1055.
[8] M. Gabelica-Robert, M. Goreaud, P. Labbe, B. Raveau, *J. Solid State Chem.* **1982**, *45*, 389.
[9] R. C. Mercader, L. Terminiello, G. J. Long, D. G. Reichel, K. Dickhaus, R. Zysler, R. Sanchez, M. Tovar, *Phys. Rev. B* **1990**, *42*, 25.
[10] Y. P. Wang, K. H. Lii, S. L. Wang, *Acta Crystallogr., Sect. C* **1989**, *45*, 1417.
[11] A. Leclaire, M. M. Borel, A. Grandin, B. Raveau, *J. Solid State Chem.* **1988**, *76*, 131.
[12] N. Lokanath, M. Sridhar, J. Prasad, G. Gopalakrishna, K. Ashamanjari, *Bull. Mater. Sci.* **2000**, *23*, 175.
[13] Q. Huang, S.-J. Hwu, *Inorg. Chem.* **1998**, *37*, 5869.
[14] F. Sanz, C. Parada, J. M. Rojo, C. Ruiz-Valero, R. Saez-Puche, *J. Solid State Chem.* **1999**, *145*, 604.
[15] F. Erragh, A. Boukhari, B. Elouadi, E. M. Holt, *J. Crystallogr. Spectrosc. Res.* **1991**, *21*, 321.
[16] L. Beaury, J. Derouet, L. Binet, F. Sanz, C. Ruiz-Valero, *J. Solid State Chem.* **2004**, *177*, 1437.
[17] I. Belharouak, P. Gravereau, C. Parent, J. P. Chaminade, E. Lebraud, G. Le Flem, *J. Solid State Chem.* **2000**, *152*, 466.
[18] F. Erragh, A. Boukhari, A. Sadel, E. M. Holt, *Acta Crystallogr., Sect. C* **1998**, *54*, 1373.
[19] F. Erragh, A. Boukhari, F. Abraham, B. Elouadi, *J. Solid State Chem.* **1995**, *120*, 23.
[20] R. G. Burns, *Mineralogical Applications of Crystal Field Theory*, Cambridge University Press, Cambridge, UK **1970**.
[21] J. F. Martin, A. Yamada, G. Kobayashi, S. Nishimura, R. Kanno, D. Guyomard, N. Dupre, *Electrochem. Solid-State Lett.* **2008**, *11*, A12.
[22] G. Kobayashi, S. Nishimura, M. Park, R. Kanno, M. Yashima, T. Ida, A. Yamada, *Adv. Funct. Mater.* **2009**, *19*, 395.
[23] C. Didier, M. Guignard, C. Denage, O. Szajwaj, S. Ito, I. Saadoune, J. Darriet, C. Delmas, *Electrochem. Solid-State Lett.* **2011**, *14*, A75.
[24] F. Sauvage, L. Laffont, J.-M. Tarascon, E. Baudrin, *Inorg. Chem.* **2007**, *46*, 3289.
[25] A. Van der Ven, M. K. Aydinol, G. Ceder, *Phys. Rev. B* **1998**, *58*, 6.
[26] S.-W. Kim, J. Kim, H. Gwon, K. Kang, *J. Electrochem. Soc.* **2009**, *156*, A635.
[27] J. L. Dodd, R. Yazami, B. Fultz, *Electrochem. Solid State Lett.* **2006**, *9*, A151.
[28] S. P. Ong, A. Jain, G. Hautier, B. Kang, G. Ceder, *Electrochem. Commun.* **2010**, *12*, 427.
[29] Y. Furushima, C. Yanagisawa, T. Nakagawa, Y. Aoki, N. Muraki, *J. Power Sources* **2011**, *196*, 2260.
[30] C. Delacourt, P. Poizot, J.-M. Tarascon, C. Masquelier, *Nat. Mater.* **2005**, *4*, 254.
[31] M.-H. Ryou, Y. M. Lee, J.-K. Park, J. W. Choi, *Adv. Mater.* **2011**, *23*, 3066.
[32] G. Kresse, *Comput. Mater. Sci.* **1996**, *6*, 15.
[33] J. P. Perdew, K. Burke, M. Ernzerhof, *Phys. Rev. Lett.* **1996**, *77*, 3865.
[34] P. E. Blöchl, *Phys. Rev. B* **1994**, *50*, 17953.
[35] S. L. Dudarev, G. A. Botton, S. Y. Savrasov, C. J. Humphreys, A. P. Sutton, *Phys. Rev. B* **1998**, *57*, 1505.
[36] F. Zhou, M. Cococcioni, C. Marianetti, D. Morgan, G. Ceder, *Phys. Rev. B* **2004**, *70*, 235121.
[37] A. Toukmaji, *Comput. Phys. Sci.* **1996**, *95*, 73.
[38] M. K. Aydinol, A. F. Kohan, G. Ceder, K. Cho, J. Joannopoulos, *Phys. Rev. B* **1997**, *56*, 1354.
[39] G. Mills, H. Jónsson, G. K. Schenter, *Surf. Sci.* **1995**, *324*, 305.
[40] S. P. Ong, V. L. Chevrier, G. Hautier, A. Jain, C. Moore, S. Kim, X. Ma, G. Ceder, *Energy Environ. Sci.* **2011**, *4*, 3680.
[41] A. Jain, G. Hautier, C. Moore, B. Kang, J. Lee, H. Chen, N. Twu, G. Ceder, *J. Electrochem. Soc.* **2012**, *159*, A622.
[42] H. J. Monkhorst, *Phys. Rev. B* **1976**, *13*, 5188.